Time-resolved absolute radius estimation of vibrating contrast microbubbles using an acoustical camera

Spiekhout, Sander; Voorneveld, Jason; Van Elburg, Benjamin; Renaud, Guillaume; Segers, Tim; Lajoinie, Guillaume P.R.; Versluis, Michel; Verweij, Martin D.; De Jong, Nico; Bosch, Johannes G.

DOI
10.1121/10.0011619

Publication date
2022

Document Version
Final published version

Published in
Journal of the Acoustical Society of America

Citation (APA)
Spiekhout, S., Voorneveld, J., Van Elburg, B., Renaud, G., Segers, T., Lajoinie, G. P. R., Versluis, M., Verweij, M. D., De Jong, N., & Bosch, J. G. (2022). Time-resolved absolute radius estimation of vibrating contrast microbubbles using an acoustical camera. *Journal of the Acoustical Society of America*, *151*(6), 3993-4003. https://doi.org/10.1121/10.0011619

Time-resolved absolute radius estimation of vibrating contrast microbubbles using an acoustical camera

Sander Spiekhout, Jason Voorneveld, Benjamin van Elburg, et al.

Citation: The Journal of the Acoustical Society of America **151**, 3993 (2022); doi: 10.1121/10.0011619
View online: https://doi.org/10.1121/10.0011619
View Table of Contents: https://asa.scitation.org/toc/jas/151/6
Published by the Acoustical Society of America

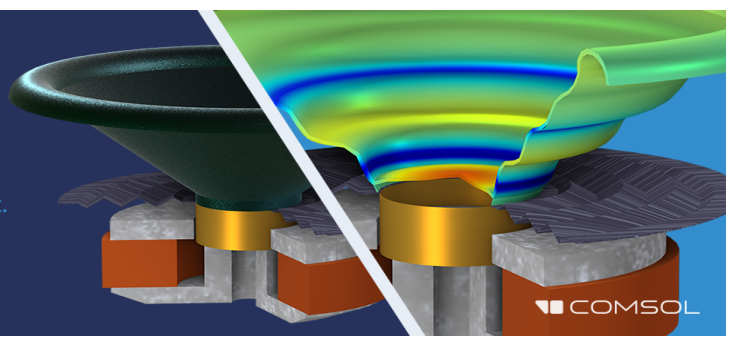

JASA ARTICLE

Time-resolved absolute radius estimation of vibrating contrast microbubbles using an acoustical camera

Sander Spiekhout,[1,a)] Jason Voorneveld,[1] Benjamin van Elburg,[2] Guillaume Renaud,[3] Tim Segers,[4] Guillaume P. R. Lajoinie,[2] Michel Versluis,[2] Martin D. Verweij,[3,b)] Nico de Jong,[3,b)] and Johannes G. Bosch[1]

[1]*Biomedical Engineering, Erasmus MC, University Medical Center Rotterdam, Rotterdam, The Netherlands*

[2]*Physics of Fluids Group, Department of Science and Technology, MESA+ Institute for Nanotechnology and Technical Medical (TechMed) Center, University of Twente, Enschede, The Netherlands*

[3]*Laboratory of Medical Imaging, Department of Imaging Physics, Delft University of Technology, Delft, The Netherlands*

[4]*Biomedical and Environmental Sensor Systems (BIOS) Lab-on-a-Chip Group, Max Planck Center for Complex Fluid Dynamics, University of Twente, Enschede, The Netherlands*

ABSTRACT:

Ultrasound (US) contrast agents consist of microbubbles ranging from 1 to 10 μm in size. The acoustical response of individual microbubbles can be studied with high-frame-rate optics or an "acoustical camera" (AC). The AC measures the relative microbubble oscillation while the optical camera measures the absolute oscillation. In this article, the capabilities of the AC are extended to measure the absolute oscillations. In the AC setup, microbubbles are insonified with a high- (25 MHz) and low-frequency US wave (1–2.5 MHz). Other than the amplitude modulation (AM) from the relative size change of the microbubble (employed in Renaud, Bosch, van der Steen, and de Jong (2012a). "An 'acoustical camera' for in vitro characterization of contrast agent microbubble vibrations," Appl. Phys. Lett. **100**(10), 101911, the high-frequency response from individual vibrating microbubbles contains a phase modulation (PM) from the microbubble wall displacement, which is the extension described here. The ratio of PM and AM is used to determine the absolute radius, R_0. To test this sizing, the size distributions of two monodisperse microbubble populations ($R_0 = 2.1$ and 3.5 μm) acquired with the AC were matched to the distribution acquired with a Coulter counter. As a result of measuring the absolute size of the microbubbles, this "extended AC" can capture the full radial dynamics of single freely floating microbubbles with a throughput of hundreds of microbubbles per hour.

 https://doi.org/10.1121/10.0011619

(Received 7 January 2022; revised 18 May 2022; accepted 20 May 2022; published online 14 June 2022)

[Editor: Charles C. Church] Pages: 3993–4003

I. INTRODUCTION

Microbubbles (MBs) are widely used for enhancing the contrast in ultrasound (US) diagnostic imaging for visualization of the blood pool in US images (Christensen-Jeffries *et al.*, 2020; Frinking *et al.*, 2020; Lindner, 2004; Stride *et al.*, 2020). The bubbles are typically 1–10 μm in diameter with a high molecular weight gas core and a phospholipid or polymer shell. Studying their resonance behavior in US fields is critical for improving MB-aided US imaging techniques. MB resonance is determined by their size and the mechanical shell properties (Versluis *et al.*, 2020). Typically, MBs are characterized using bulk measurements, which effectively integrates all individual bubble responses into one (Alsadiq *et al.*, 2021; Segers *et al.*, 2016; Segers *et al.*, 2018). However, it is known that MBs of the same size can exhibit significantly different acoustic responses—even when derived from the same bubble population—because of differences in shell properties (Luan *et al.*, 2016; Sijl *et al.*, 2011). To assist research on improved MB formulations and contrast imaging techniques, we investigate the vibrational behavior of individual MBs under different driving conditions. Individual MB spectroscopy (van der Meer *et al.*, 2007) is typically realized with ultra-high-frame-rate optical imaging (Chin *et al.*, 2003), but this method typically necessitates a constraining boundary, which changes the behavior (Wang and Manmi, 2014). Furthermore, optical imaging of MBs is complex, expensive, and labor intensive (Renaud *et al.*, 2014), rendering it impractical for characterizing the vibration behavior of a large collection of single MBs (Segers *et al.*, 2016).

A purely acoustical apparatus for studying the radial dynamics of individual MBs, called the "acoustical camera" (AC), was proposed by Renaud *et al.* (2014, 2012a,b). The principle of the AC relies on the fact that high-frequency (HF) sound waves (far above the resonance frequency of the MB) do not induce MB vibration but are passively scattered with an amplitude proportional to the MB radius (Renaud *et al.*,

[a)]Electronic mail: s.spiekhout@erasmusmc.nl

[b)]Also at: Biomedical Engineering, Erasmus MC, University Medical Center Rotterdam, Rotterdam, the Netherlands.

2012a). Therefore, the volumetric oscillation of the MB driven by a low-frequency (LF) pulse will cause an *amplitude modulation* (AM) of the scattered HF amplitude. Amplitude demodulation (ADM) of this scattered HF probing signal enables the measurement of the MB's relative vibrational amplitude or radial strain, $\Delta R/R_0$. The principle and technical details of the AC used in this study are developed in Sec. II.

Although the AC is a useful instrument due to its technical simplicity and high throughput, a downside is its inability to measure the resting radius, R_0, directly. Without a quantification of R_0, the characterization capabilities are limited as it is impossible to distinguish the effects of size from shell properties on the MB resonance behavior. Even for state-of-the-art monodisperse MBs (van Elburg *et al.*, 2021), the variation in R_0 is such that the mean radius, $\overline{R_0}$, cannot be safely used to substitute the single bubble radius, and individual sizing is needed for accurate characterization.

To overcome this limitation, several approaches have been proposed for AC setups. Chirp resonance detection has been used to derive the size of free gas bubbles (Cavaro *et al.*, 2011; Czarnecki *et al.*, 2015). The resonance of coated MBs, however, depends on coating composition (Marmottant *et al.*, 2005; Sirsi and Borden, 2009), which invalidates the method. Adding single-shot optics capabilities to an AC is possible (Luan *et al.*, 2016) but complicates the setup and measurements considerably, requiring precise alignment of the optical and acoustical foci.

A different approach, suggested by Fouan *et al.* (2015) exploits the phase modulation (PM) of the scattered pressure in an AC setup to derive the MB resting radius. This method relates phase changes in the scattered pressure signal to absolute bubble wall displacements ΔR. Combining this ΔR with $\Delta R/R_0$, obtained from the conventional AC approach, allows the estimation of R_0.

Although Fouan *et al.* (2015) measured a relation between bubble size and phase/AM, their results deviated by up to 40% from the optically measured sizes. Also, their bubble sizes ranged between 40 and 120 μm in radius, far above the limit for clinically relevant MB sizes (Sennoga *et al.*, 2012).

In this paper, we describe our AC principle and setup (Sec. II B), provide a complete physical description of the PM effect that we exploit here (Sec. III), describe the measurement methods (Sec. IV), present the results (Sec. V), discuss their implications (Sec. VI), and summarize the main findings (Sec. VII).

II. ACOUSTICAL CAMERA FOR STUDYING MB VIBRATIONS

A. Principle of acoustical camera

A schematic of the AC principle is shown in Fig. 1. A probing wave with carrier frequency, f_c, which by far exceeds the first-order volumetric resonance frequency of typical MBs, is directed to the sample. When such a HF wave is scattered by a single MB, the scattered pressure amplitude will scale linearly with instantaneous MB size (Renaud *et al.*, 2012a). For a vibrating bubble, the HF scattered pressure will be AM by the MB's radial dynamics, and these can be derived by the ADM of the scattered HF signal.

In the AC setup (Fig. 2), a small tank with three transducers, the focal spots of the two orthogonally placed HF transducers overlap in a small (~8 nL; 200 μm^3) focal region. The suspension of MBs circulating inside the AC tank is highly diluted so that it is statistically unlikely to have more than one bubble within the focal region at any time. Mild stirring assures that the region is refreshed before the arrival of the next probing pulse.

The bubble vibration is induced by a LF transducer aligned to the same focal point, driven by a series of LF pulses in the frequency range of the bubble resonance; this LF sequence is synced to the HF probing pulse. The effect of specific waveforms on individual MBs can, thus, be studied, including the (sub)harmonic response to broadband pulses, and chirps, etc. This method allows hundreds or thousands of individual MB measurements per hour, which is at least an order of magnitude faster than optical methods (Renaud *et al.*, 2014). Additionally, this technique has superior temporal resolution and can record acquisitions of up to hundreds of microseconds per bubble, whereas ultra-high-speed imaging methods are typically limited to 128 frames. The ADM of the scattered HF signal, in principle, allows the monitoring of the relative vibrational response of any vibrating scatterer induced by any arbitrary waveform.

B. Acoustical camera setup

In the AC setup used here, shown schematically in Fig. 2, a HF probing wave with a frequency, f_c, of 25 MHz and a peak-to-peak pressure of 500 kPa is transmitted from an angle $\theta = 0°$, and the scattering from the bubble is recorded at $\theta = 90°$. The 20 kPa LF wave with modulation frequency, f_m, between 1.0 and 2.5 MHz is transmitted from $\theta = 225°$ to

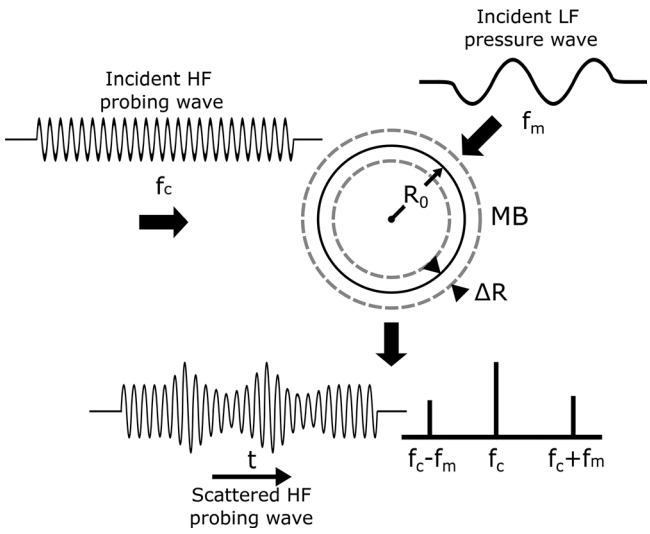

FIG. 1. Principle of the AC. An individual MB of resting radius, R_0, vibrates with wall displacement, ΔR, as a function of incident LF pressure wave with frequency, f_m. A HF wave with frequency, f_c, probes the MB, which results in a scattered HF field that is AM as a function of the radial dynamics of the MB.

https://doi.org/10.1121/10.0011619

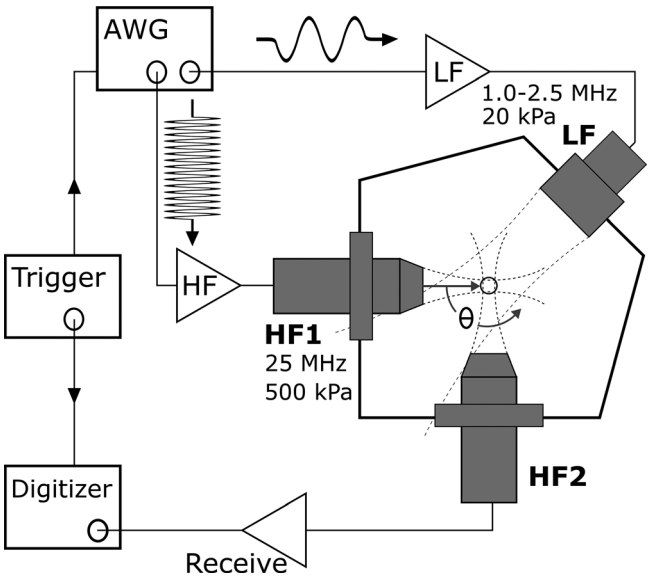

FIG. 2. Schematic of the full AC setup. A focused HF transducer (HF1) transmits the HF pulse at angle $\theta = 0°$, which probes the MB in focus. The scattered HF signal is received by the second HF transducer (HF2) at $\theta = 90°$. The MB in the shared focal zone vibrates as a function of the LF signal transmitted by the LF transducer.

drive the bubble oscillation. It should be noted that the MB also scatters the LF wave, but this falls outside the bandwidth of the receiving transducer. The length of the LF signal is always 20 μs shorter than the HF to allow two 10 μs reference HF scattering signal sections before and after the MB vibrations.

The HF and LF signals are generated by an arbitrary waveform generator (AWG; WW2572A, 250 MS/s, Tabor Electronics, Tel Hanan, Israel) and amplified (150A100B, Amplifier Research, Bothell, WA and 310 L, ENI, Rochester, NY). These signals are transmitted with a pulse repetition frequency of 15 s^{-1}, following a trigger signal from a second AWG (33220A, Agilent, Palo Alto, CA). The same trigger signal starts the recording of the scattered HF signal, which is then amplified (AU-151910289, Miteq, Hauppauge, NY) and digitized (M4x.4420-x4, Spectrum Instrumentation, Limerick, Ireland). The recorded signals are stored on an external hard drive and processed on a separate workstation using MATLAB (The MathWorks, Natick, MA).

The suspension inside the tank is a phosphate-buffered saline solution, stirred by a magnetic stirrer platform (MR 2000, Heidolph Instruments, Schwabach, Germany). Stirring-induced speed is estimated to be on the order of 10 mm/s and, thus, much higher than the expected 25 μm/s from Brownian motion (Putri and Redhyka, 2017). These velocities are, in turn, negligible with respect to the bubble wall velocities of 50 cm/s. The foci of all three transducers are aligned by a pulse echo technique localizing a 1 mm diameter needle. For the two HF transducers (V324, Olympus Industrial, Essex, UK), this mainly comprises a rotation to counteract the eccentricity of the ultrasonic beam. For the LF transducer (PA275, Precision Acoustics, Dorchester, UK), this is a matter of finding the right distance. After calibration, the needle is removed. The effective focal zone where bubbles can be probed is estimated to have a size of 8 nL.

III. PROPERTIES OF SCATTERED HF SIGNAL

A. Theory of scattering by small spheres

The scattering from a fluid or gaseous sphere with dimensions on the order of the acoustic wavelength was first calculated by Anderson (1950). This scattering model incorporates compressibility and gas properties and can produce the scattered pressure at a given angle. Johnson (1977) showed that this scattering model, at low ratios of wavelength to scattering dimensions, converges to the Rayleigh scattering solution. The model predicts a quasi-linear relation between bubble radius and scattered amplitude and phase. This model does not incorporate shell effects and fluid viscosity. However, these are expected to have little effect on the HF scattering behavior as the frequencies are far above the first-order volumetric resonance frequency (Hoff *et al.*, 2000).

The presumed linear relation underlying the AC's working principle is (Renaud *et al.*, 2012a)

$$\frac{\Delta R}{R_0} \approx m, \tag{1}$$

where m is the normalized vibrational amplitude. Second, we assume a similar (quasi-) linear relation between scattered phase, $\Delta\varphi$, and ΔR. To verify both assumptions, we use Anderson's solution for scattering from a fluid sphere (Anderson, 1950) as implemented by Baddour (2021). We apply parameters corresponding to our AC setup: the f_c is set to 25 MHz, the pressure is set to 500 kPa, and the gas properties of perfluorobutane are used to calculate the HF scattered pressure and HF scattered phase 25 mm from the scattering MB's center at a receiving θ of 90°. Scatter radii, R, range from 1 to 6 μm. The result is shown in Fig. 3. To highlight the quasi-linear trends between the radius and the scattered pressure amplitude and scattered pressure phase, a linear relation with the pressure at $R_0 = 3.5$ μm, P_0, is plotted in the same graphs. This demonstrates the linear relationship between bubble size and scattered HF pressure [Fig. 3(A)] and between bubble size and scattered HF phase [Fig. 3(B)]. The deviations from the linear trend around bubble radii of 2.35, 3.14, 5.11, and 5.41 μm in Fig. 3 are not numerical errors but can be attributed to higher-order resonance modes (Sage *et al.*, 1979). It is unknown whether these resonances occur for highly damped lipid-shelled MBs. No indication for this behavior was found experimentally in this study.

The phase behavior is related to a varying distance from the bubble wall to receiver, essentially a time-of-flight difference. It should be realized that this phase relation as a function of the radius is different for each scattering θ, and only seems to be quasi-linear for θ close to 90° as can be seen in Fig. 4(B).

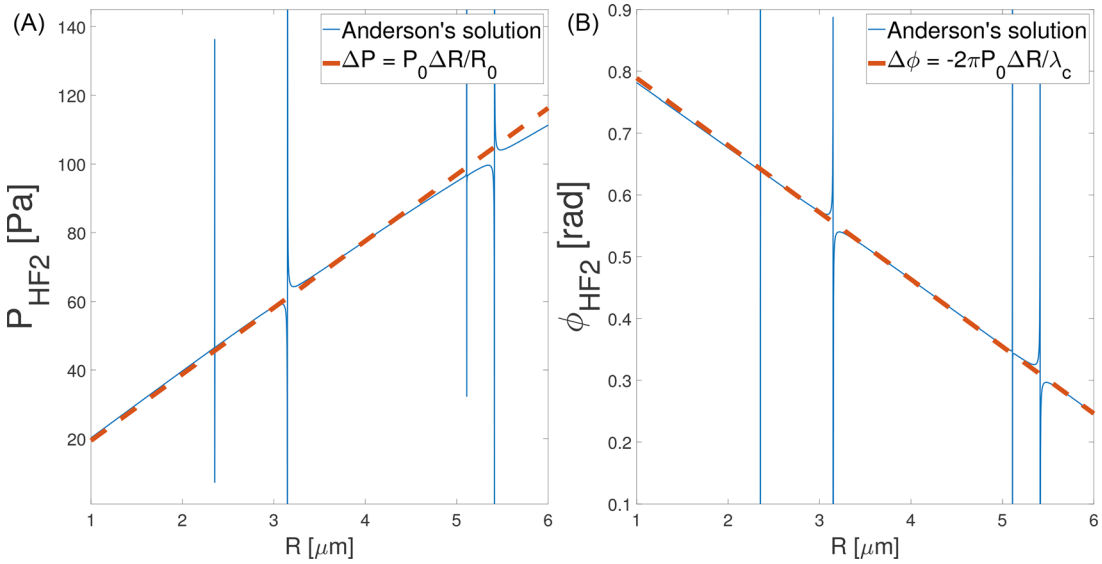

FIG. 3. (Color online) The (A) HF scattered pressure amplitude from a MB as a function of the bubble radius, modeled by the fluid sphere solution from Anderson, with a linear relation overlayed in red (Anderson, 1950), and (B) HF scattered pressure phase calculated with the same model are shown. The spikes at $R = 2.4$, 3.1, 5.1, and 5.4 μm can be attributed to higher-order resonance modes (Sage *et al.*, 1979).

In Fig. 4(B), the scattered pressure phase is compared to the smallest scatter size ($R = 1$ μm) at θ of 90°. From this, we can see that MBs with a $R \geq 2$ μm do not act as a spherical wave point source but scatter higher pressure amplitudes in the forward direction. We see a similar effect in the scattered phase difference, where the spherical asymmetry increases for larger MB sizes, although the phase differences decrease in the forward direction.

Redoing these calculations for lower f_c results in more spherically symmetric scattering behavior, indicating we are on the edge of the Rayleigh scattering regime. From these asymmetric scattering profiles, it should be realized that our proposed phase-based sizing method should take this angle-dependent radius-phase relation into account, which will be different for a different HF transducer configuration and probing frequency.

Having identified the given quasi-linear relation between scattering (phase and amplitude) and instantaneous bubble size, we derive expressions for the AM and PM effects in Appendix A. From this, we find that the MB's R_0 can be isolated from

$$R_0 = \frac{\Delta\varphi}{m}\frac{c}{\omega_c}, \tag{2}$$

where $\Delta\varphi$ is the modulation phase of the HF scattered signal, ω_c is the angular frequency of the probing pulse, and c is the speed of sound in the medium.

Here, it is worth mentioning that the PM effect on the acoustic scattering from a pulsating sphere was already derived by Censor (1984, 1988), which sparked a strong debate on confounding PM effects (Censor, 1986; Piquette and Van Buren, 1986; Piquette *et al.*, 1988) that ultimately led to identifying some limiting cases where the PM effect employed here is the dominant one. In this study, we are in such a limiting case as the scatterer dimension is small compared to the probing wavelength. And, thus, the technique of measuring the MB wall displacement—as described here—can be seen as a practical application of Censor's acoustical Doppler effect.

IV. METHODS

A. MB sizing experiments

To verify the validity of the sizing method, first, a validation of the complete signal processing was performed using synthetic signals as generated by vibrating bubbles, following the assumptions of Eq. (A11). The accuracy of the detected radial strain and MB radius was assessed for ideal harmonic bubble oscillations, more complex compression-only vibrations (de Jong *et al.*, 2007), and different levels of noise. This validation is fully described in Appendix B.

Second, MB measurements were executed using the setup described in Sec. II B, which is shown schematically in Fig. 2. A monodisperse MB suspension was formed in a flow-focusing device operated at 55 °C (Segers *et al.*, 2019) using a phospholipid mixture comprising DSPC and DPPE-PEG5000 (Corden Pharma, Liestal, Switzerland; molar ratio of 9:1) and a gas mixture of 12 vol.% of C_4F_{10} in CO_2, exactly as in Segers *et al.* (2020). Then, 100 nL of the suspension was added to the 210 ml of phosphate-buffered saline solution in the tank. This results in a MB concentration of approximately 1 bubble per 10 mm^3. Two MB populations with $\overline{R_0} = 2.1$ μm ($MB_{2.1}$) and $\overline{R_0} = 3.5$ μm ($MB_{3.5}$) were used. The measurements were stopped after 20 min as time affects MB behavior due to gas diffusion. Prior to performing the AC measurements, MB populations were sized, and their concentrations were determined using a Coulter counter (CC) Multisizer 3 (Beckman Coulter, Mijdrecht, The Netherlands), equipped with a 50 μm aperture tube, allowing quantification of particle sizes from R_0 0.5 to 15 μm.

https://doi.org/10.1121/10.0011619

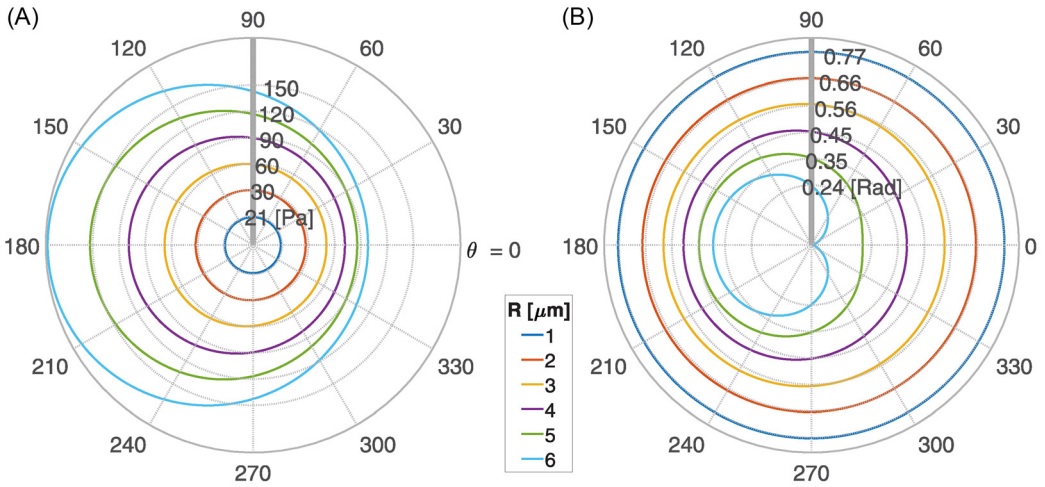

FIG. 4. (Color online) The angle dependence of HF scattered pressure for different MB sizes as simulated by the fluid sphere scattering model of Anderson. The (A) polar plot of HF scattered pressure amplitude and (B) polar plot of HF scattered pressure phase are shown. The calculations are for different values of R_0 from 1 to 6 μm. The incident wave enters from the right and $\theta = 0°$ represents backscattering, and the gray line at 90° corresponds with the receiving HF transducer's angle.

To verify the stability of MB size in suspension, sizing of the MB sample was repeated 20 times over the course of 20 min.

B. Excitation signals

The LF pulse is shown in Fig. 5. The LF signal spans five frequencies around the bulk resonance of the $MB_{2.1}$, which was observed during attenuation measurements, to increase the chance of inducing MB vibrations. The pressure level of 20 kPa is selected as it results in modestly high MB vibrational amplitudes, avoiding bubble destruction while providing sufficient vibrational amplitude. Each individual pulse is 12 cycles long and Hanning-tapered over the first and last cycles. The alternating frequency order and 10 μs dead time are incorporated to avoid interference between the MB responses to successive pulses (Czarnecki *et al.*, 2015).

For the size measurements of the smaller $MB_{2.1}$, the LF signal spans the frequencies from 1.5 to 2.5 MHz. For the larger $MB_{3.5}$ the frequencies are lowered by 500 kHz as the expected resonance lowers with increasing size.

C. Signal processing

An example of a measured MB signal appears in Fig. 6(A). We define the SNR as the ratio of the mean square values (modulus) of the first 10 μs of the (unmodulated) HF signal to a 10 μs section of the signal measured after HF transmission. The received signals are analyzed if their SNR is at least 30 dB, which ensures that the bubble is in the focal zone. The received signal shows the response to the train of five excitation signals, colored in Fig. 6(A), separated in time by 10 μs, which are analyzed independently by demodulation. The signal before, between, and after the pulses, depicted in gray in Fig. 6(A), should contain no modulation and are used to calculate the reference HF scattering levels. The signals where these reference levels vary by more than 25% over the entire 100 μs are excluded as

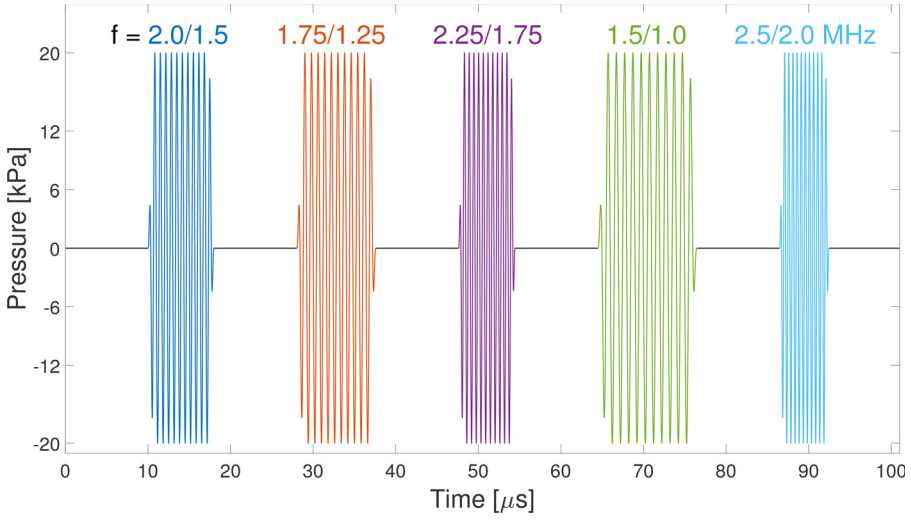

FIG. 5. (Color online) The pulse sequence used in the experiments to size the MBs. Alternating frequencies are selected around the ensemble resonance, and a modest pressure amplitude of 20 kPa was used to avoid altering MB properties. For the $MB_{2.1}$, the higher frequencies (2.0, 1.75, etc.) are used. For the $MB_{3.5}$, the lower frequencies (1.5, 1.25, etc.) are used.

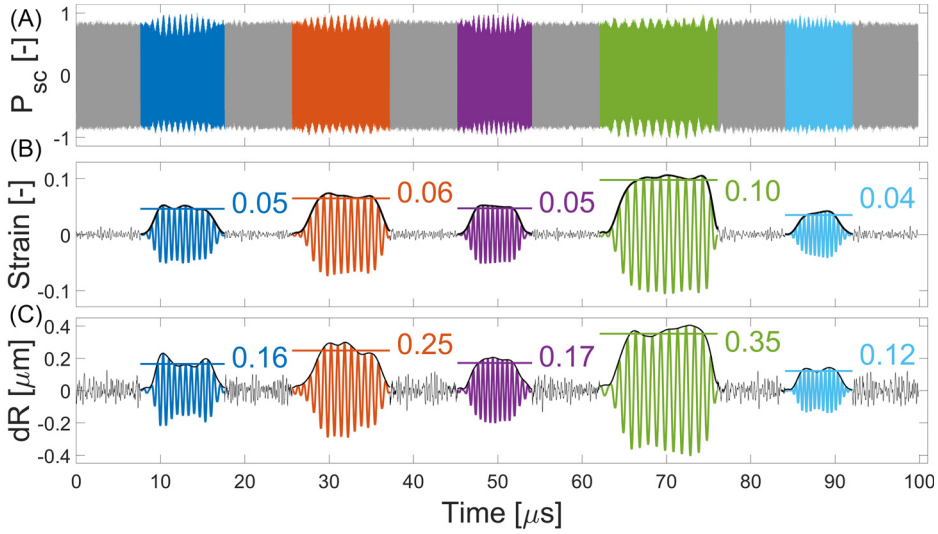

FIG. 6. (Color online) The (A) measured HF scattered signal from a single MB is shown, where gray regions indicate reference sections in the absence of the LF signal and colored regions mark the LF signals. Here, color coding corresponds to Fig. 5, and LF driving frequencies for each section are labeled. (B) The ADM strain signal appears with the modulus of the analytical signal indicating the strain magnitude. The horizontal line with label indicates the measured strain magnitude. (C) The PDM ΔR signal appears with similar dynamics as the ADM envelope but significantly noisier. The horizontal line with label indicates the measured ΔR magnitude, which can be divided by the strain magnitude from (B) to obtain an R_0 estimate.

this indicates that the MB is moving through or away from the focus. The five sections containing oscillating MB signals are bandpass filtered with cut-off values of $f_c \pm 2.5 \times f_m$ to include MB dynamics up to the second harmonic following Eq. (A11). The filtered signal sections are then Hilbert transformed to compute the analytic signal.

ADM is realized following:

$$\frac{|H(P_{sc})| - |H(\mathrm{HF_{ref}})|}{|H(\mathrm{HF_{ref}})|}, \tag{3}$$

where P_{sc} is the signal received by the HF transducer, and $|H(\,)|$ denotes the modulus of the analytic signal. The mean scattering level, $|H(\mathrm{HF_{ref}})|$, is the average of the modulus of the analytic signal of the two adjacent reference sections. The m magnitude is determined as the maximum of the $\Delta R(t)/R_0$ (i.e., *strain*) signal in the frequency domain.

Phase demodulation (PDM) is executed by calculating the instantaneous phase of the complex analytical signal (applying the atan2 routine in MATLAB). This phase is then compared to the phase of an ideal numerical sine wave of frequency, f_c, sampled at the same time points to obtain the isolated PM signal. Phase signals typically drift slowly due to slow MB translation through the tank and are significantly noisier than strain signals. The ΔR amplitude is determined as the maximum magnitude in a frequency range around f_m. The ratio of ΔR amplitude to m amplitude yields a unique R_0 estimate for each of the five individual LF pulses. For the sizing procedure, R_0 estimates with $m < 0.05$ were excluded because of low SNR: a weak bubble vibration was found to result in unreliable phase quantification.

An example of the *strain*-time, and ΔR-time curves are displayed in Figs. 6(B) and 6(C) to show the similar dynamics for both signals. For this example, a bandpass filter of $f_m \pm 350$ kHz was applied to the demodulated LF sections to ensure a zero mean level in the ΔR-time and *strain*-time signals. The demodulated reference levels in Figs. 6(B) and 6(C) are high-pass filtered from 1.5 MHz. In the demodulated time signals, a horizontal line is plotted through the magnitudes of the *strain* and ΔR as determined by the demodulation scheme. To illustrate the sizing method on Fig. 6, ΔR and the *strain* magnitudes are used to calculate, following Eq. (2), four R_0 estimates ($m \geq 0.05$) with a mean of 3.57 μm and a standard deviation (STD) of $\pm$ 0.42 μm.

V. RESULTS

From the bubble dynamics simulations, included in Appendix B, it was found that noise-free scattering yields an accurate sizing (error $< 1\%$) for all bubble sizes between 1 and 6 μm. The presence of noise affects the PDM (radius) more than the ADM (strain). According to the simulations, this will lead to an overestimation of the radius and a higher variance, especially for small bubbles. For the $\mathrm{MB_{2.1}}$, an absolute sizing error of 8% is expected with a STD of 15% when SNR = 30 dB. For the larger $\mathrm{MB_{3.5}}$, the expected absolute sizing error is 5% with a deviation of approximately 8.5%.

The acoustical sizing method was validated experimentally on the two monodisperse MB populations. A total of 161 and 169 valid MB signals were recorded and processed for the $\mathrm{MB_{2.1}}$ and $\mathrm{MB_{3.5}}$, respectively. From these individual MB signals, on average, 45.6% of the $\mathrm{MB_{2.1}}$ and 48.2% of the $\mathrm{MB_{3.5}}$ LF sections passed the m threshold of 0.05 and were used to create the size distributions shown by the blue bars in Fig. 7. The AC distributions were then fitted to a Gaussian distribution, which is depicted by the yellow line. The monodisperse MB sizes can by approximated by a Gaussian distribution because the controlled circumstances within the microfluidic device should produce bubbles of the same radius with a small random variation. The time-averaged CC results are shown by the red line, and to demonstrate the stability over time, the CC of the first and last minute are denoted by the purple and green lines, respectively. The CC distribution in Fig. 7(B) shows numerous particles of $1 \leq R_0 \leq 1.5$ μm, which we speculate to be lipid

https://doi.org/10.1121/10.0011619

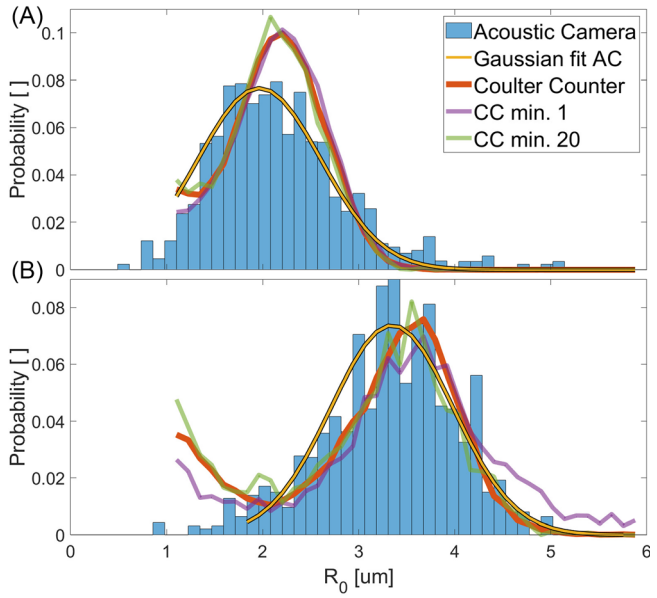

FIG. 7. (Color online) The (A) probability of MB size distribution from 161 individual MB recordings displayed by blue bars with a Gaussian fit displayed by the yellow line is shown. The time-averaged size distribution of the $MB_{2.1}$ as measured by the CC displayed by the three lines appears, where red corresponds to the time average, purple corresponds to the first minute, and green corresponds to the last minute. (B) AC ($n = 169$) and CC data measured from $MB_{3.5}$ are shown.

aggregates that increased in size during transport due to convection.

The accuracy of estimating the peak, R_0, was compared by using a Gaussian fit on the AC and CC distribution, from which a 4.6% underestimation was found for the larger $MB_{3.5}$. For the smaller $MB_{2.1}$, we found an underestimation of 8%. The precision of the sizing method was compared to the CC by using the full width at half-maximum (FWHM), which was overestimated by 6% for the $MB_{3.5}$, and 19% for the $MB_{2.1}$. For the individual statistics, we refer to Table I. The similarity between AC- and CC-sized distributions was investigated by applying a χ^2 test to the size distributions. The difference between the corresponding AC and CC distributions were found to be statistically insignificant ($p = 0.23$ for $MB_{2.1}$, $p = 0.24$ for $MB_{3.5}$).

VI. DISCUSSION

A. Performance of the AC for MB sizing

The sizing method was applied to two monodisperse MB populations of different sizes, and over 160 individual MBs were successfully measured for both sizes. This demonstrates that this new approach can recover the size distribution measured with a CC. The larger MBs were sized with a higher precision and accuracy than the smaller MBs. This was expected because the sizing method relies on an accurate estimation of the PM index, which is more reliable for larger MB. As shown in Fig. 3, the scattered HF amplitude scales linearly with the bubble size, whereas the thermal noise remains constant; the SNR, thus, increases linearly with the bubble size. Signals with higher SNR yield a more accurate PM index. Additionally, for the same m, an increased MB size results in a larger absolute displacement of the wall, which translates into a larger PM on the probing signal.

TABLE I. The peak and FWHM values are calculated from the Gaussian fit on the size distributions shown in Fig. 7 with P scores from a χ^2 test.

	AC ($\overline{R_0}$/FWHM) (μm)	CC ($\overline{R_0}$/FWHM) (μm)	p value (χ^2 test)
$MB_{2.1}$	1.98/1.44 ($n = 161$)	2.15/1.21 ($n = 10\,000$)	0.24
$MB_{3.5}$	3.35/1.38 ($n = 169$)	3.51/1.30 ($n = 3500$)	0.23

For the AC sizing performance, the m threshold is important, but the SNR threshold is critical. We experimentally confirmed that if the SNR threshold is lowered, unreliable size estimates are taken into account, resulting in an AC-obtained size distribution that widens and deviates considerably from the CC size distribution. The m threshold has a similar but weaker effect. An increase in either the SNR or m thresholds leads to a rejection of more MB signals and, thus, to a sparser and less smooth distribution.

The SNR of the setup could be increased by transmitting a higher HF pressure amplitude or lowering the f-number in receive, leading to a better sizing performance, as well as to a more reliable capture of the relative radial dynamics. Another potential improvement in sizing performance follows from a higher HF transmit frequency, which will lead to a larger PM index. However, the HF frequency should remain within the limits of the Rayleigh scattering regime (scatterer dimension $<$ wavelength/10) for the bubble sizes under investigation, otherwise. the linear relation of MB size with scattered HF pressure amplitude and phase would no longer hold. A higher m can be achieved by increasing the modulating pressure amplitude, but this raises the risk of altering the MBs within its acoustic path. In fact, a possible improvement is to minimize this irradiation by generating a trigger only when the backscattered HF level is sufficiently high, therefore, the LF pulse is transmitted only when a MB is in focus.

B. Perspectives

In its original manifestation, the AC was already capable of studying dynamic MB responses through ADM but lacked the capability of measuring the resting radius, R_0. In this novel method, the AC can measure the full radial dynamics of individual MB—without sacrificing the ease of operation associated with the original setup. This means that the AC can now be used for full characterization of the nonlinear MB shell on an individual basis. The realized throughput of ~160 bubbles measured per hour is much higher than optical imaging systems, where around 5–10 bubbles per hour are typically measured (Faez *et al.*, 2011). This throughput is lower, though, than earlier work (Renaud *et al.*, 2012a) from the higher required SNR threshold.

Another potential use of the system is to assess the range and cause of differences in acoustic responses of MBs

with comparable sizes. Considerable differences in response have been reported for polydisperse MBs with marginal size differences (Luan *et al.*, 2016). It would be particularly interesting to investigate this aspect for monodisperse MB because their formation process is more stringently controlled.

C. Limitations of the study

In this study, we have limited ourselves to two sizes of (relatively large) monodisperse MBs. Although it is obvious that there is a lower limit to the sizes of MBs that can be measured in the AC, we did not yet explore this limit explicitly. The current, f_c, of 25 MHz is expected to induce vibrations only to MB with $R_0 < 0.7\,\mu$m, which poses a limit to the sizable range. This limit can be overcome by increasing f_c. In the current setting, the loss of accuracy restricts the sizing to MBs with radi i > 1–2 μm, e.g., the minimum detectable MB size is determined by the overall SNR of the system. Increasing this will likely allow for smaller MBs to be studied with an AC and make the AC a more versatile setup for studying MB vibrations. This remains the subject of further research.

Commercial contrast agents are polydisperse ($R_0 = 0.5$–$5\,\mu$m) and will require a wider f_m range than the one used here. We have recently shown (Spiekhout *et al.*, 2021) that a wider frequency range (1–5 MHz) and a 50 kPa driving pressure can be used for that purpose. The smaller bubbles ($R_0 \sim 0.5\,\mu$m) are abundantly present, although they may not contribute to the overall response. Removing them by filtering, decantation, or acoustic sorting provides ways of separating the bubbles that can be investigated by the current AC (Spiekhout *et al.*, 2021). Because the smallest ($R_0 = 0.5\,\mu$m) bubbles' HF scattering pressure is expected to be reduced sevenfold compared to the larger MBs studied here ($R_0 = 3.5\,\mu$m), the SNR should be increased accordingly. Increasing the HF pressure seven times introduces nonlinear propagation, therefore, the required SNR increase for studying MBs down to this size should be achieved with a combination of a higher probing pressure, reduced focal distance of both HF transducers, and a more sensitive receiver.

Although we demonstrated the sizing principle here, the purpose of the AC setup remains to study individual MB behavior and not act as a sizing tool. With this sizing technique, the AC can capture the full radial dynamics [$R(t)$] instead of just the relative change [$(\Delta R/R_0)(t)$].

VII. CONCLUSION

Here, we made the AC a more complete setup for studying single MB vibrations by adding the capability of quantifying the resting radius. The MBs are sized by employing the phase and AM of HF scattering from a single vibrating MB. For this sizing method, a theoretical framework was described and validated using simulations. We confirmed the validity of this sizing principle by showing a good agreement between size distributions obtained with this acoustical sizing method and a CC measurement of the same MB population. This validation was conducted on two distinct monodisperse MB populations. We achieved good agreement with Coulter counter measurements of the same sample with a 4.6% underestimation of the AC-obtained size distribution for the larger $MB_{3.5}$ and a widening of 6%. For the smaller $MB_{2.1}$, there was an 8% underestimation and 19% widening. We attribute the better performance for larger bubbles to an increase in SNR that follows from a larger scattering cross section.

Having demonstrated the sizing technique, the AC is now capable of capturing the full radial dynamics of individual freely floating MBs in response to a given acoustic pulse.

ACKNOWLEDGMENTS

This publication is part of the project Bubble-X of the research program Ultra-X-Treme (P17-32), which is financed by the Dutch Research Council (NWO). We would like to thank Robert Beurskens for advice and technical assistance and Paul van Neer for his helpful comments regarding phase transfer characterization.

APPENDIX A: AMPLITUDE AND PM OF HF SCATTERING BY A MB VIBRATING AT A LOWER FREQUENCY

Without loss of generality, we assume a harmonically pulsating spherical MB with an instantaneous radius,

$$R(t) = R_0 + \Delta R\,\sin(\omega_m t). \tag{A1}$$

When exposed to the HF probing wave, the MB scatters an omnidirectional pressure field with amplitude, P, angular frequency, ω_c, and phase, φ. Here, ω_m is the bubble pulsation angular frequency. The subscripts, c and m, denote the carrier and modulation, respectively. Assuming a linear relation between the radius and scattered pressure as argued above, a change in instantaneous radius, $R(t)$, from R_0 to $R_0 + \Delta R$ leads to a pressure AM given by m. The instantaneous scattered pressure, $p(t)$, is then given by

$$p(t) = P_0[1 + m(t)]\sin(\omega_c t), \tag{A2}$$

where

$$m(t) = m\sin(\omega_m t) \tag{A3}$$

is the modulation signal, and P_0 is the unmodulated scattered HF amplitude. The pressure given in Eq. (A2) can be rewritten as

$$p(t) = P_0\sin(\omega_c t) + \frac{1}{2}P_0 m\cos[(\omega_c - \omega_m)t] - \frac{1}{2}P_0 m\cos[(\omega_c + \omega_m)t], \tag{A4}$$

which is a classical AM signal with equal sidebands at frequencies $\omega_c \pm \omega_m$ of amplitude $m/2$ relative to P_0, i.e.,

$$m = \frac{\Delta R}{R_0}. \tag{A5}$$

https://doi.org/10.1121/10.0011619

We will now derive the phase change of the scattered pressure from a harmonically pulsating MB. Assuming the initial phase $\varphi_0 = 0$, the PM on the scattered pressure, $p(t)$, is given by

$$p(t) = P_0 \sin(\omega_c t + \varphi(t)). \tag{A6}$$

Here, $\varphi(t)$ is the instantaneous phase given as

$$\varphi(t) = \Delta\varphi \sin(\omega_m t), \tag{A7}$$

where the PM magnitude, $\Delta\varphi$, is given by (as seen from Fig. 3)

$$\Delta\varphi = -\Delta R \frac{\omega_c}{c}, \tag{A8}$$

where c is the speed of sound in water. Using goniometric relations and identities 9.1.42 and 9.1.43 from Abramowitz and Stegun, (1974), Eqs. (A6) and (A7) can be combined and reduced to find

$$p(t) = P_0 \sum_{n=-\infty}^{\infty} J_n(\Delta\varphi) \sin(\omega_c t + n\omega_m t), \tag{A9}$$

where J_n is the nth Bessel function of the first kind. Note that $m(t)$ can be retrieved by ADM and $\varphi(t)$ can be retrieved by PDM of the scattered signal, therefore, using Eqs. (A5) and (A8) and assuming a quasi-linear relation between m and $\Delta\varphi$ with ΔR, we can, in principle, isolate R_0 from

$$R_0 = \frac{\Delta\varphi}{m}\frac{c}{\omega_c}. \tag{A10}$$

The AM and PM effects occur simultaneously, which can be expressed by combining Eq. (A2) and the $n = -1$, 0, and 1 terms (which is valid if weak PM is assumed, i.e., small $\Delta\varphi$) of Eq. (A9) to find

$$p(t) = P_0 \sin(\omega_c t) + \frac{1}{2} P_0 M \sin[(\omega_c + \omega_m)t - \alpha] - \frac{1}{2} P_0 M \sin[(\omega_c - \omega_m)t - \alpha], \tag{A11}$$

where

$$M = \sqrt{(\Delta\varphi^2 + m^2)}, \tag{A12}$$

and

$$\alpha = \arctan\left(\frac{m}{\Delta\varphi}\right). \tag{A13}$$

However, from Eq. (A11), it may be noticed that $\Delta\varphi$ and m occur at the same frequency, and demodulation of the detected signal is required. This relation also emphasizes the need for a flat phase transfer function of the HF receiving transducer, which we verified to be the case by using a reflection-based calibration procedure (van Neer *et al.*, 2011).

APPENDIX B: VALIDATION OF SIGNAL PROCESSING USING SYNTHETIC SIGNALS

1. Demodulation

The demodulation schemes, explained in Sec. IV, were tested on synthetic signals representing the scattering of vibrating MBs to verify that the reconstructed signal matches the imposed radial dynamics. To illustrate, a simple MB vibration signal with R_0 of 3 μm and m of 0.2 is constructed, which is shown in Fig. 8(A). The scattered pressure from this MB is modeled using Eq. (A11) with amplitude P_0 set to 1, f_c set to 25 MHz, and sample rate, F_s, set to 250/s, resulting in the pressure signal shown in Fig. 8(B). The critical features of the ADM routine—the pressure envelope in green, the reference scattering level in purple, and derived from that, strain $\Delta R/R_0$ in red—are highlighted in the same plot.

The PM effect on the scattered pressure is invisible on this time scale. However, isolating the phase of the scattered signal and subtracting the phase of an unmodulated sine wave with $f = f_c$ yields a sine signal in sync with the modulated pressure envelope and periodic with f_m. From this, the amplitude of $\Delta\varphi$ is determined, and using Eq. (A10), R_0 is found. Multiplication with $\Delta R/R_0 + 1$ yields the radial dynamics displayed in Fig. 8(C). Here, the minimum radius is reconstructed within 0.5% of the imposed value.

A more complex, compression-only MB $R(t)$ curve (Sijl *et al.*, 2011), which includes a subharmonic component, was created using

$$R = R_0 - m R_0 \left(\sin(\omega_m t) + \sin\left(\frac{\omega_m}{2} t\right)\right)^2,$$

with R_0 set to 3.6 μm, and m set to 0.11, the result of which is displayed in Fig. 8(D). Repeating the steps as above, the scattered signal is constructed [Fig. 8(E)], then demodulated, and reconstructed to find the radial dynamics shown in Fig. 8(F). This example shows that compression-only and subharmonics can be reconstructed while retaining the excellent (<0.5% deviation) accuracy.

2. Accuracy

Demodulation accuracy was determined systematically for R_0 from 1 to 6 μm in 100 steps, and m values range from 0.01 to 0.2 in 40 steps, using the method showcased in Figs. 8(A)–8(C). All of the signals were constructed with an f_c of 25 MHz, a 12 cycle modulation wave with f_m of 2 MHz, with white Gaussian noise added at a SNR of 30 dB. These signals were then ADM and PDM to retrieve values for $\Delta R/R_0$, ΔR, and R_0. Each $R_0 - m$ combination was simulated 25 times to assess how the randomness of the noise affects the spread in sizing accuracy.

Preliminary experiments with MB $\overline{R_0}$ of 2 μm showed that 30 dB noise levels are realistic. Furthermore, noise showed to be mostly of electrical origin and, thus, approximately constant. Because the HF scattering amplitude scales with R_0 (Renaud *et al.*, 2012a), it would be more realistic to use a size-dependent SNR or fixed noise level, but for showing the

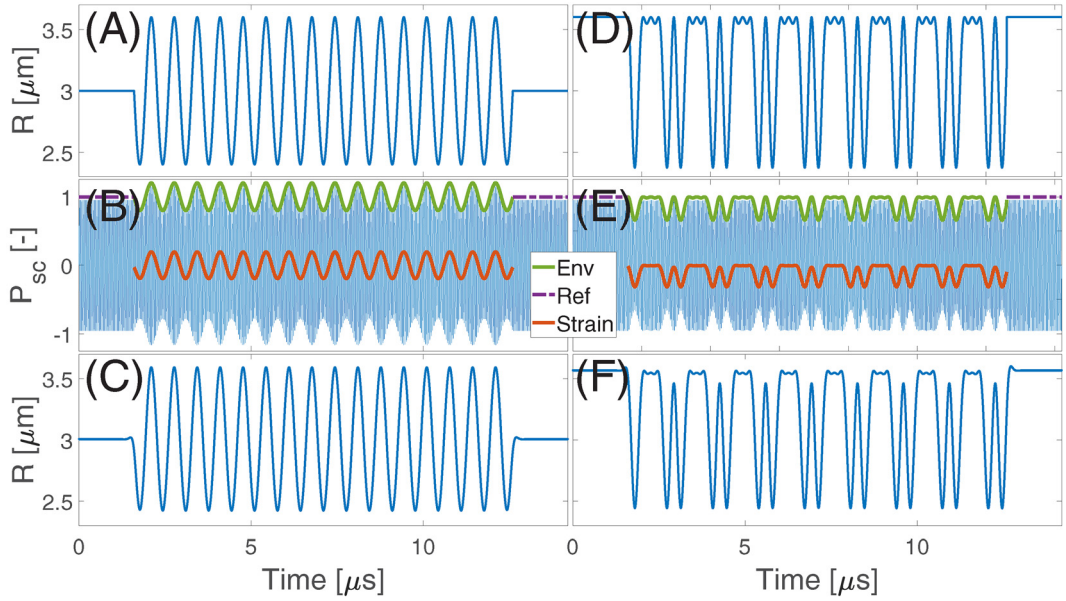

FIG. 8. (Color online) The steps involved in simulating the demodulation process. (A) and (D) show a simple and complex input bubble radius-time curve, respectively. From these signals, a noise-free HF scattering signal is constructed with AM and PM using Eq. (A11), shown in (B) and (E). The critical features for ADM are highlighted. The reconstructed bubble $R(t)$ curve from demodulating (B) and (E) are displayed in (C) and (F), respectively..

dependence on size, the fixed SNR is more suitable. In principle—given enough transmitted HF pressure amplitude—a 30 dB SNR can be achieved for any size.

3. Results

From demodulating synthetic, noise-free signals, the size estimation error remained within 1% for R_0 from 1 to 6 μm if m exceeds 0.02. Adding white Gaussian noise decreases the size estimation accuracy considerably, as can be seen from Fig. 9(A).

Here, the darkest blue region corresponds with R_0 overestimation over 20%. Size estimation errors of 5% are indicated by the dashed red line, which for R_0 of 3.5 μm is at m of 0.05 but requires m of 0.082 for R_0 of 2 μm. Sizing errors of 10% are indicated by the solid green line. If PDM accuracy is assessed individually instead of the combined ADM and PDM, interchangeable results are found, which emphasizes the difference in strength of AM over PM. Decreasing the probing wavelength eventually equalizes PDM and ADM accuracy, but this is prohibited by the requirement to stay within the Rayleigh scattering regime; see Secs. III B and VI A.

Figure 9(B) shows the STD as a function of m and imposed R_0 value. Dispersion in sizing follows the trend of sizing accuracy with poor results in the bottom left corner, which improve with increasing R_0 and m. Here, a relative STD of 10% and 15% are indicated by the dashed red and green lines, respectively.

From Fig. 9, it can be deduced that measuring MB with R_0 of 2.0 μm and a minimum m of 0.05 results in a sizing error of approximately 8% and a deviation of 15%. For a MB with R_0 of 3.5 μm, the expected error is just above 5% and the deviation is around 8.5%. Although these errors are higher than state-of-the art MB sizing methods such as optical microscopy and Coulter counting (1.1% and 4.3%,

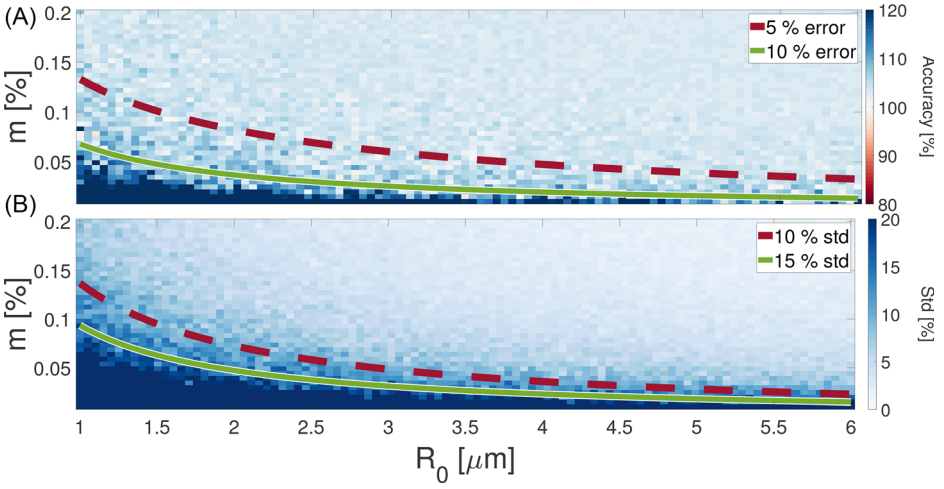

FIG. 9. (Color online) (A) The estimated R_0 accuracy from the sizing method on synthetic signal $R(t)$ curve relative to the imposed R_0 value is shown. The dashed red line indicates a 5% error level, and the solid green line shows the 10% error level. (B) The STD in sizing accuracy calculated from repeating simulations 25 times are expressed relative to imposed R_0. Here, 10% deviation is shown by the dashed red line, and 15% deviation is indicated by the solid green line.

respectively; Sennoga *et al.*, 2012), for this proof-of-principle sizing technique, we consider these levels acceptable, and we foresee further accuracy improvements by reducing the HF propagation length in receive and by increasing the HF pressure levels. As *in vitro* sizing experiments include signals SNR $\geq$ 30 dB, sizing should outperform the estimates from this model.

Abramowitz, M., and Stegun, I. (**1974**). *Handbook of Mathematical Functions, with Formulas, Graphs, and Mathematical Tables* (U.S. GPO, Washington, DC).

Alsadiq, H., Tupally, K., Vogel, R., Kokil, G., Parekh, H. S., and Veidt, M. (**2021**). "Shell properties and concentration stability of acoustofluidic delivery agents," Phys. Eng. Sci. Med. **44**(1), 79–91.

Anderson, V. C. (**1950**). "Sound scattering from a fluid sphere," J. Acoust. Soc. Am. **22**(4), 426–431.

Baddour, R. E. (**2021**). "MATLAB implementation of Anderson's solution of sound scattering from a fluid sphere (Anderson, V.V., JASA 22:426-431, 1950)," available at http://www.ieee-uffc.org/ultrasonics/software.asp (Last viewed April 30, 2021).

Cavaro, M., Payan, C., Moysan, J., and Baqué, F. (**2011**). "Microbubble cloud characterization by nonlinear frequency mixing," J. Acoust. Soc. Am. **129**(5), EL179–EL183.

Censor, D. (**1984**). "Harmonic and transient scattering from time varying obstacles," J. Acoust. Soc. Am. **76**(5), 1527–1534.

Censor, D. (**1986**). "Reply to 'Comments on " 'Harmonic and transient scattering from time varying obstacles" [J. Acoust. Soc. Am. **76**, 1527–1534 (1984)],' " J. Acoust. Soc. Am. **79**(1), 181–182.

Censor, D. (**1988**). "Acoustical Doppler effect analysis—Is it a valid method?," J. Acoust. Soc. Am. **83**(4), 1223–1230.

Chin, C. T., Lancée, C., Borsboom, J., Mastik, F., Frijlink, M. E., De Jong, N., Versluis, M., and Lohse, D. (**2003**). "Brandaris 128: A digital 25 million frames per second camera with 128 highly sensitive frames," Rev. Sci. Instrum. **74**(12), 5026–5034.

Christensen-Jeffries, K., Couture, O., Dayton, P. A., Eldar, Y. C., Hynynen, K., Kiessling, F., O'Reilly, M., Pinton, G. F., Schmitz, G., Tang, M.-X., Tanter, M., and van Sloun, R. J. (**2020**). "Super-resolution ultrasound imaging," Ultrasound Med. Biol. **46**(4), 865–891.

Czarnecki, K., Fouan, D., Achaoui, Y., and Mensah, S. (**2015**). "Fast bubble dynamics and sizing," J. Sound Vib. **356**, 48–60.

de Jong, N., Emmer, M., Chin, C. T., Bouakaz, A., Mastik, F., Lohse, D., and Versluis, M. (**2007**). " 'Compression-only' behavior of phospholipid-coated contrast bubbles," Ultrasound Med. Biol. **33**(4), 653–656.

Faez, T., Emmer, M., Docter, M., Sijl, J., Versluis, M., and de Jong, N. (**2011**). "Characterizing the subharmonic response of phospholipid-coated microbubbles for carotid imaging," Ultrasound Med. Biol. **37**(6), 958–970.

Fouan, D., Achaoui, Y., Payan, C., and Mensah, S. (**2015**). "Microbubble dynamics monitoring using a dual modulation method," J. Acoust. Soc. Am. **137**(2), EL144–EL150.

Frinking, P., Segers, T., Luan, Y., and Tranquart, F. (**2020**). "Three decades of ultrasound contrast agents: A review of the past, present and future improvements," Ultrasound Med. Biol. **46**(4), 892–908.

Hoff, L., Sontum, P. C., and Hovem, J. M. (**2000**). "Oscillations of polymeric microbubbles: Effect of the encapsulating shell," J. Acoust. Soc. Am. **107**(4), 2272–2280.

Johnson, R. K. (**1977**). "Sound scattering from a fluid sphere revisited," J. Acoust. Soc. Am. **61**(2), 375–377.

Lindner, J. R. (**2004**). "Microbubbles in medical imaging: Current applications and future directions," Nat. Rev. Drug Discov. **3**(6), 527–533.

Luan, Y., Renaud, G., Raymond, J. L., Segers, T., Lajoinie, G., Beurskens, R., Mastik, F., Kokhuis, T. J. A., van der Steen, A. F. W., Versluis, M., and de Jong, N. (**2016**). "Combined optical sizing and acoustical characterization of single freely-floating microbubbles," Appl. Phys. Lett. **109**(23), 234104.

Marmottant, P., van der Meer, S., Emmer, M., Versluis, M., de Jong, N., Hilgenfeldt, S., and Lohse, D. (**2005**). "A model for large amplitude oscillations of coated bubbles accounting for buckling and rupture," J. Acoust. Soc. Am. **118**(6), 3499–3505.

Piquette, J. C., and Van Buren, A. L. (**1986**). "Some further remarks regarding scattering of an acoustic wave by a vibrating surface," J. Acoust. Soc. Am. **80**(5), 1533–1536.

Piquette, J. C., Van Buren, A. L., and Rogers, P. H. (**1988**). "Censor's acoustical Doppler effect analysis—Is it a valid method?," J. Acoust. Soc. Am. **83**(4), 1681–1682.

Putri, I. E., and Redhyka, G. G. (**2017**). "Theoretical investigation on particle Brownian motion on micro-air-bubble characteristic in H_2O solvent," IOP Conf. Ser: Mater. Sci. Eng. **214**(1), 012003.

Renaud, G., Bosch, J. G., Van Der Steen, A. F., and De Jong, N. (**2014**). "Low-amplitude non-linear volume vibrations of single microbubbles measured with an 'acoustical camera,' " Ultrasound Med. Biol. **40**(6), 1282–1295.

Renaud, G., Bosch, J. G., van der Steen, A. F. W., and de Jong, N. (**2012a**). "An 'acoustical camera' for *in vitro* characterization of contrast agent microbubble vibrations," Appl. Phys. Lett. **100**(10), 101911.

Renaud, G., Bosch, J. G., van der Steen, A. F. W., and de Jong, N. (**2012b**). "Chirp resonance spectroscopy of single lipid-coated microbubbles using an 'acoustical camera,' " J. Acoust. Soc. Am. **132**(6), EL470–EL475.

Sage, K. A., George, J., and Überall, H. (**1979**). "Multipole resonances in sound scattering from gas bubbles in a liquid," J. Acoust. Soc. Am. **65**(6), 1413–1422.

Segers, T., de Jong, N., and Versluis, M. (**2016**). "Uniform scattering and attenuation of acoustically sorted ultrasound contrast agents: Modeling and experiments," J. Acoust. Soc. Am. **140**(4), 2506–2517.

Segers, T., Gaud, E., Casqueiro, G., Lassus, A., Versluis, M., and Frinking, P. (**2020**). "Foam-free monodisperse lipid-coated ultrasound contrast agent synthesis by flow-focusing through multi-gas-component microbubble stabilization," Appl. Phys. Lett. **116**(17), 173701.

Segers, T., Gaud, E., Versluis, M., and Frinking, P. (**2018**). "High-precision acoustic measurements of the nonlinear dilatational elasticity of phospholipid coated monodisperse microbubbles," Soft Matter **14**(47), 9550–9561.

Segers, T., Lassus, A., Bussat, P., Gaud, E., and Frinking, P. (**2019**). "Improved coalescence stability of monodisperse phospholipid-coated microbubbles formed by flow-focusing at elevated temperatures," Lab Chip **19**(1), 158–167.

Sennoga, C. A., Yeh, J. S., Alter, J., Stride, E., Nihoyannopoulos, P., Seddon, J. M., Haskard, D. O., Hajnal, J. V., Tang, M.-X., and Eckersley, R. J. (**2012**). "Evaluation of methods for sizing and counting of ultrasound contrast agents," Ultrasound Med. Biol. **38**(5), 834–845.

Sijl, J., Overvelde, M., Dollet, B., Garbin, V., de Jong, N., Lohse, D., and Versluis, M. (**2011**). " 'Compression-only' behavior: A second-order nonlinear response of ultrasound contrast agent microbubbles," J. Acoust. Soc. Am. **129**(4), 1729–1739.

Sirsi, S. R., and Borden, M. A. (**2009**). "Microbubble compositions, properties and biomedical applications," Bubble Sci., Eng. Technol. **1**(1-2), 3–17.

Spiekhout, S., Voorneveld, J., Renaud, G., van Elburg, B., Segers, T., Versluis, M., Verweij, M., de Jong, N., and Bosch, J. (**2021**). "Acoustical sizing of individual microbubbles using an 'acoustical camera,' " Erasmus MC, Rotterdam, pp. 117–120, available at https://www.echocontrast.nl/archive/ (Last viewed May 6, 2021).

Stride, E., Segers, T., Lajoinie, G., Cherkaoui, S., Bettinger, T., Versluis, M., and Borden, M. (**2020**). "Microbubble agents: New directions," Ultrasound Med. Biol. **46**(6), 1326–1343.

van der Meer, S. M., Dollet, B., Voormolen, M. M., Chin, C. T., Bouakaz, A., de Jong, N., Versluis, M., and Lohse, D. (**2007**). "Microbubble spectroscopy of ultrasound contrast agents," J. Acoust. Soc. Am. **121**(1), 648–656.

van Elburg, B., Collado-Lara, G., Bruggert, G.-W., Segers, T., Versluis, M., and Lajoinie, G. (**2021**). "Feedback-controlled microbubble generator producing one million monodisperse bubbles per second," Rev. Sci. Instrum. **92**(3), 035110.

van Neer, P. L., Vos, H. J., and de Jong, N. (**2011**). "Reflector-based phase calibration of ultrasound transducers," Ultrasonics **51**(1), 1–6.

Versluis, M., Stride, E., Lajoinie, G., Dollet, B., and Segers, T. (**2020**). "Ultrasound contrast agent modeling: A review," Ultrasound Med. Biol. **46**(9), 2117–2144.

Wang, Q. X., and Manmi, K. (**2014**). "Three dimensional microbubble dynamics near a wall subject to high intensity ultrasound," Phys. Fluids **26**(3), 032104.